Milky Way Survey (10°≤l$ $20°) 13CO & C18O Dense Structure Morphological Analysis Post-print

Authors: Xiao Yanshan, Zhang Haixia, Huang Yao, Jiang Zhibo, Chen Zhiwei, Zheng Sheng, Zhang Peng, Luo Xiaoyu, Jiang Yu, Pan Xuejiao

Date: 2025-10-11T00:00:00+00:00

Abstract

Dense molecular cloud clumps are the sites of star formation, and their morphological characteristics are closely related to the physical properties of molecular gas. This study is based on data observed with the 13.7 m millimeter-wave radio telescope at Purple Mountain Observatory, covering a galactic longitude (l) range of 10°≤l 20°*andagalacticlatitude*(b$) range of $|b| \leqslant 5^{\circ}.25$, to conduct morphological classification and analysis of dense structures in 13CO(J=1−0) and C18O(J=1−0). Using the FacetClumps detection algorithm, we detected and manually verified molecular cloud cores traced by C18O spectral line data, obtaining a total of 544 C18O molecular cloud cores. Approximately 5.97% of the 13CO clumps in this region contain C18O cores. We divided the 13CO clumps into two categories based on the presence or absence of C18O cores, finding that the peak intensity, flux, and angular area of 13CO clumps containing C18O cores are significantly larger than those of the sample of 13CO clumps without C18O cores, while no significant differences were found in the eccentricity and shape factor between the two samples. Additionally, we performed a comparative analysis of the shape factors of 13CO clumps and C18O cores, showing that the velocity-integrated intensity contours of C18O cores are significantly closer to circular morphology.

Full Text

Morphological Analysis of Dense 13CO & C18O Structures in the Milky Way Imaging Scroll Painting (10° ≤ l ≤ 20°)

XIAO Yan-shan[1,2], ZHANG Hai-xia[1,2], HUANG Yao[1,2]†, JIANG Zhi-bo[3], CHEN Zhi-wei[3], ZHENG Sheng[1,2], ZHANG Peng[1,2], LUO Xiao-yu[1,2], JIANG Yu[3], PAN Xue-jiao[1,2]

[1]Center for Astronomy and Space Sciences, China Three Gorges University, Yichang 443002
[2]College of Mathematics and Physics, China Three Gorges University, Yichang 443002
[3]Purple Mountain Observatory, Chinese Academy of Sciences, Nanjing 210023

Abstract

Dense molecular clumps are the sites of star formation, and their morphological characteristics are closely linked to the physical properties of the molecular gas. This study is based on data obtained with the Purple Mountain Observatory 13.7 m millimeter-wave radio telescope, covering the region with galactic longitudes (l) $10° \leq l \leq 20°$ and galactic latitudes (b) $|b| \leq 5°$. We focus on the classification and morphological analysis of dense structures traced by 13CO(J=1−0) and C18O(J=1−0) emission lines. Using the FacetClumps detection algorithm, we detected and manually verified molecular cores traced by the C18O spectral line data, obtaining a total of 544 C18O molecular cores. Approximately 5.97% of the 13CO clumps in this region contain C18O cores. We categorized the 13CO clumps based on the presence or absence of C18O cores and found that those containing C18O cores have significantly higher peak intensities, fluxes, and angular areas compared to those without C18O cores. However, no significant differences in eccentricity or form factor were found between the two categories. Furthermore, a comparative analysis of form factor shows that the velocity-integrated intensity contours of C18O cores are notably closer to circular shapes than those of 13CO clumps.

Key words stars: formation, ISM: molecules, ISM: lines and bands, methods: data analysis

1 Introduction

The discovery and observation of interstellar molecules have profoundly impacted modern astronomy by establishing that stars form in molecular clouds. Molecular clouds exhibit complex hierarchical structures that can be subdivided into substructures such as clouds, clumps, and cores. Based on extensive observational results, the current paradigm posits that star formation occurs in dense molecular clouds. Molecular clouds undergo quasi-static contraction to form filamentary structures, and under certain physical conditions, when these filaments become sufficiently dense, they fragment into molecular clumps of various sizes, shapes, and density structures. When the density and mass of a molecular clump reach critical values such that it can no longer resist gravitational collapse, it begins to contract and form protostellar objects. Dense molecular clumps are thus the cradles of star formation, and their morphological and physical characteristics determine the initial conditions for star formation, making them important subjects of study.

In molecular clouds, the primary constituent is molecular hydrogen (H_2). Aside

from H_2, carbon monoxide (CO) is the most abundant and important molecule. CO serves as the most widely used molecular probe for investigating the physical state, distribution, and kinematic properties of molecular clouds. Different CO isotopologues with varying optical depths can effectively probe different layers and environments within the interstellar medium. In particular, the completely optically thin C18O molecule provides opportunities to study smaller or denser regions that are typically closest to or about to undergo star formation.

To comprehensively understand the distribution of molecular gas in the Galactic plane, numerous CO molecular line surveys of Galactic structure have been conducted both domestically and internationally, including the Harvard-Smithsonian Center for Astrophysics CO(J=1-0) survey, the Five College Radio Astronomy Observatory Galactic Ring Survey (GRS), the 13CO/C18O Heterodyne Inner Milky Way Plane Survey (CHIMPS) from the Astrophysics Research Institute of Liverpool John Moores University, the Structure, Excitation and Dynamics of the Inner Galactic Interstellar Medium (SEDIGISM) survey from the Max Planck Institute for Radio Astronomy, and the Milky Way Imaging Scroll Painting (MWISP) survey from the Purple Mountain Observatory of the Chinese Academy of Sciences. These survey projects have yielded massive observational datasets, enabling astronomers to conduct numerous meaningful studies on the relationship between the properties of Galactic molecular gas and star formation.

Yuan et al. correlated cloud morphology, properties, and Galactic environment by classifying clouds into filamentary and non-filamentary structures, finding that approximately 10% of filamentary molecular clouds contribute about 90% of the total CO flux. Neralwar et al. first completed morphological classification of molecular cloud data from the SEDIGISM survey using the J-plots algorithm and visual inspection, finding that most clouds exhibit elongated structures. Subsequently, Clarke et al. updated the classification labels for the SEDIGISM catalog using an improved RJ-plots algorithm, demonstrating a strong correlation between the central concentration of molecular cloud structures and their star formation efficiency as well as dense gas fraction, but no significant correlation with filamentary morphology. These studies selected larger-scale CO molecular clouds as classification objects to analyze morphological characteristics and patterns.

In recent years, the vigorous development of machine learning technology has enhanced the performance of detection algorithms for small-scale dense structures in molecular clouds. For example, the GaussClumps algorithm obtains clump regions through iterative three-dimensional Gaussian fitting at maximum peaks; the ClumpFind detection algorithm uses contour levels to assign pixels containing extremum points to that extremum as a dense structure; the Fell-Walker algorithm finds local maxima by following the direction of maximum gradient from points of lower intensity, assigning all points converging at the same peak position to the same structure; and the Dendrograms algorithm displays the hierarchical structure of molecular spectral lines, identifying molecu-

lar clumps by constructing hierarchical structures. Additionally, new detection algorithms specifically designed for molecular clumps and cores have emerged, such as Local Density Clustering, which uses local density clustering methods to determine clump centers, members, and boundaries; ConBased, which divides signals into small regions and uses connectivity-based merging rules considering peak distance, intensity differences, and volume; and FacetClumps, which applies multivariate function extremum theorems to determine cluster centers and combines connectivity with minimum distance to cluster local regions divided by local gradients, demonstrating high accuracy for dense structure detection. These improved detection methods have produced extensive catalogs of dense molecular structures, providing data sources for studying the morphological characteristics of small-scale molecular clumps and cores.

The large-scale, unbiased, and high-sensitivity CO spectral line data from the MWISP survey provide an opportunity for systematic studies of the spatial distribution and morphological characteristics of molecular clumps. In this paper, we utilize the FacetClumps algorithm to detect and verify C18O molecular cores in the region with galactic longitudes $10° \leq l \leq 20°$ and galactic latitudes $|b| \leq 5°$. Combining this with the 13CO molecular clump catalog for this region, we complete the matching of 13CO clumps and C18O cores. Based on the matching results, we conduct classification studies and statistical analyses of the morphology of 13CO molecular clumps and also explore morphological differences in gas structures traced by different density probes.

This paper is organized as follows: Section 2 describes the acquisition and matching of the 13CO molecular clump and C18O molecular core samples. Section 3 presents statistical analysis of parameters for two categories of 13CO clumps based on whether they are matched with C18O cores. In Section 4, we analyze and discuss the morphological characteristics of 13CO clumps and C18O cores. Section 5 presents our conclusions.

2 Data and Methods

2.1 Data Sources

The Milky Way Imaging Scroll Painting (MWISP) is an unbiased survey project conducted with the Purple Mountain Observatory 13.7 m telescope, simultaneously observing three transition lines: CO, 13CO, and C18O(J=1-0). It features high sensitivity, a wide velocity range, and high resolution. According to the observational strategy, the survey uses a sideband-separating superconducting spectroscopic array receiver system. This receiver employs double-sideband superconductor-insulator-superconductor mixers with a fast Fourier transform spectrometer, extensively utilizing digital technology. Combined with On-The-Fly (OTF) observing mode, it demonstrates excellent operational stability and efficiency. CO is observed in the upper sideband with a main beam width of 50 , while 13CO and C18O have a beam width of 49 , both with a bandwidth of 1000 MHz and 16384 channels. The velocity resolution is approximately 0.159

km · s^{-1} for CO and 0.166 km · s^{-1} for 13CO and C18O. The entire survey covers a sky area of 10° ≤ l ≤ 250°, |b| ≤ 5°, comprising 10,941 tiles, with each tile measuring 30 × 30 . After baseline calibration of the spectral lines, three-dimensional data cubes for CO, 13CO, and C18O are produced with a grid spacing of 30 . The typical root mean square (rms) noise levels for CO, 13CO, and C18O spectral lines are 0.47 K, 0.22 K, and 0.21 K, respectively.

2.2 Data Samples

2.2.1 13CO Molecular Clumps Luo et al. utilized 13CO(J=1-0) emission line data from MWISP to extract molecular clumps and assign confidence levels for the region 10° ≤ l ≤ 20°, |b| ≤ 5° (cumulative coverage area of approximately 100 deg^2) following the Facet-SS-3D-Clump pipeline. The FacetClumps algorithm obtains candidate molecular clumps, which are cross-matched with clumps detected by the Dendrograms algorithm to obtain high-confidence clumps. These high-confidence clumps are then used as prior knowledge to train a semi-supervised deep clustering model (SS-3D-Clump), and the trained model is applied to verify candidate clumps, providing confidence levels for them. The final catalog containing 18,757 13CO clumps is published at https://www.scidb.cn/en/s/qEfe2m. This region encompasses very active massive star-forming regions such as M16, M17, W31, W33, and W39, containing numerous samples of molecular clumps and cores at different evolutionary stages, making it a key region for understanding star evolution processes. The 13CO clumps used in this paper are selected from this catalog. presents the parameters of the molecular clumps used in our statistical analysis. The clump confidence (Confidence) and clump flux (Flux) parameters in Table 1 serve as selection criteria.

The distribution of clump confidence is shown in

, ranging from 0.8 to 1.0. To ensure the reliability of the 13CO molecular clump sample, we select clumps with confidence levels greater than or equal to 0.9 as our study objects, i.e., Confidence ≥ 0.9. The flux distribution is shown in

. According to the completeness test results in the literature, when the flux is 37 K · km · s^{-1}, the clump recall rate is 90%. To ensure the completeness of our 13CO clump sample, we select clumps with flux greater than 37 K · km · s^{-1} as our study objects, i.e., Flux > 37 K · km · s^{-1}. When both selection criteria are satisfied simultaneously, we obtain 7,097 13CO molecular clumps from the catalog for analysis.

2.2.2 C18O Molecular Cores Following the 13CO molecular clump extraction method described in the literature, we employ the same FacetClumps algorithm to detect candidate C18O molecular cores in this region. FacetClumps combines a facet model with multivariate function extremum theorems to automatically locate source centers within preprocessed signal regions and uses a connectivity-based minimum-distance clustering method to merge local regions

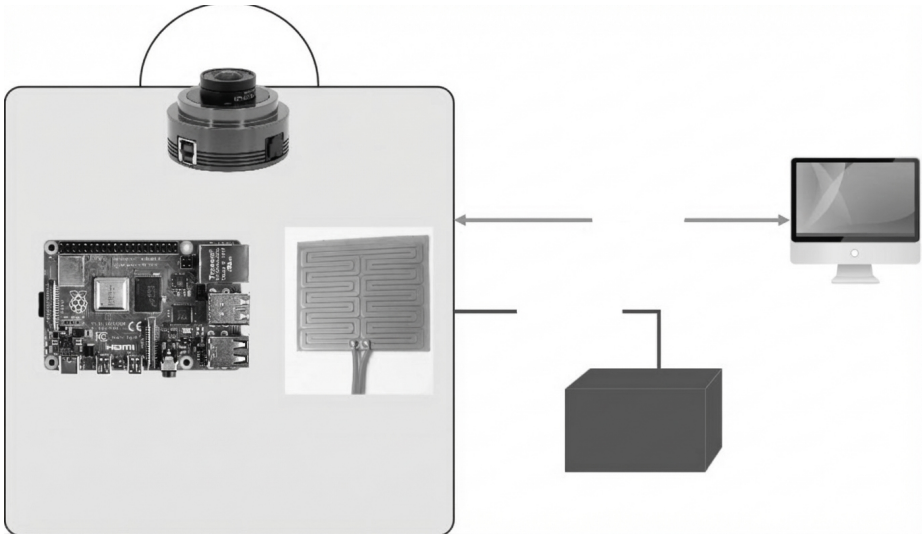

Figure 1: Figure 1

Figure 2: Figure 2

segmented by local gradients, thereby identifying regions corresponding to each source. This algorithm demonstrates high accuracy for detecting dense structures. provides the parameters for the C18O spectral line detection algorithm.

The algorithm outputs both a source catalog and mask data. The source catalog provides relevant parameters for each source, including spatial coordinate indices in the mask data; the centroid positions in galactic longitude, latitude, and radial velocity; source size; peak intensity; and flux. In the mask, pixels belonging to the same source are labeled with the same integer, while unassigned pixels are labeled as 0. Based on the centroid position and size recorded in the source catalog, we can extract the original three-dimensional data cube for each source from the input data.

Due to noise, the detection results from FacetClumps still contain a certain number of false C18O targets. After obtaining the detection catalog, manual verification is required to ensure the reliability of the C18O cores. For each C18O core candidate in the algorithm output catalog, we produced verification images showing integrated intensity maps and spectral line plots in the longitude-latitude, longitude-velocity, and latitude-velocity planes. Candidates satisfying both of the following criteria were identified as genuine C18O cores: (1) the integrated intensity maps in the first row of the verification image show a concentrated morphology; (2) both the average spectrum (second row) and maximum spectrum (third row) show clear emission peaks.

As shown in FIGURE:3, this C18O core verification image satisfies both criteria and is therefore identified as a genuine C18O core. In FIGURE:3, the integrated map is not concentrated and the spectral lines show no clear emission peaks; in FIGURE:3, the integrated map is concentrated but the spectral lines show no clear emission peaks; and in FIGURE:3, the integrated map is not concentrated but the spectral lines show clear emission peaks. Therefore, categories (b), (c), and (d) are identified as false C18O cores.

During the verification process, we adopted a three-person voting strategy. Each candidate was independently verified by three individuals, and a candidate was marked as a genuine C18O core when at least two of the three considered it real. This process yielded a total of 544 genuine C18O cores. presents a portion of the core catalog.

2.2.3 Matching 13CO Clumps with C18O Cores We matched the 7,097 13CO molecular clumps with the 544 C18O molecular cores based on their three-dimensional spatial positions. If the centroid of a C18O core fell within the boundary of a 13CO clump, the match was considered successful, meaning that the clump contains a C18O core. The 13CO clump boundaries were determined from the masks provided by FacetClumps (see Section 2.2.2). Following this procedure, we completed the matching for all 13CO clumps. The results are summarized in , with the total number of 13CO clumps matched with C18O cores shown in the first row. The matching ratio is defined as Matching Number

divided by Sample Number.

Among all 544 C18O molecular cores, only two were not matched to corresponding 13CO clumps. Analysis of these two C18O cores revealed that 13CO clumps exist at their positions, but their confidence levels are below 0.9 and therefore not included in our selected 13CO clump sample (see Section 2.2.1).

Within the specified velocity range, a total of 424 13CO clumps contain C18O cores, with some 13CO clumps matching multiple C18O cores.

and [FIGURE:5] illustrate the positional relationships and matching numbers. In

(a), blue and magenta triangles indicate that the current 13CO clump contains two C18O cores. In FIGURE:5, only a blue triangle indicates that the current 13CO clump contains one C18O core. Statistical analysis shows that 78% of 13CO clumps have one C18O core, 17% have two C18O cores, and the remaining 5% have more than two C18O cores ([FIGURE:6]).

These matching results demonstrate that all C18O cores are contained within 13CO clumps, confirming that the optically thin C18O molecular probe can trace denser substructures within molecular clumps.

3 Statistical Analysis of 13CO Clump Parameters

Based on the matching results from Section 2, we performed a binary classification of the 13CO clumps according to the presence or absence of C18O cores. The 424 13CO clumps containing C18O cores (from) are designated as "Match C18O clumps" (M-type), while the remaining 13CO clumps are designated as "No Match C18O clumps" (NM-type).

To investigate differences between these two categories, we conducted statistical analysis and comparison of their distribution in the Galactic plane, peak intensities, fluxes, and velocity spans.

3.1 Position Distribution

We examined the differences in Galactic position between the two categories through probability density functions in galactic longitude, latitude, and radial velocity.

As shown in FIGURE:7, colored lines represent the mean longitudes of different massive star-forming regions. Both categories show concentration trends in star-forming regions in longitude distribution. However, due to the much smaller number of M-type clumps, their peak positions show less consistency with star-forming regions compared to the more numerous NM-type clumps.

In FIGURE:7, within the latitude range of -5.25° to 5.25°, both M-type and NM-type clumps appear concentrated in the range (-3°, 3°), but M-type clumps are more concentrated at latitude 0°, i.e., the central region of the Galactic

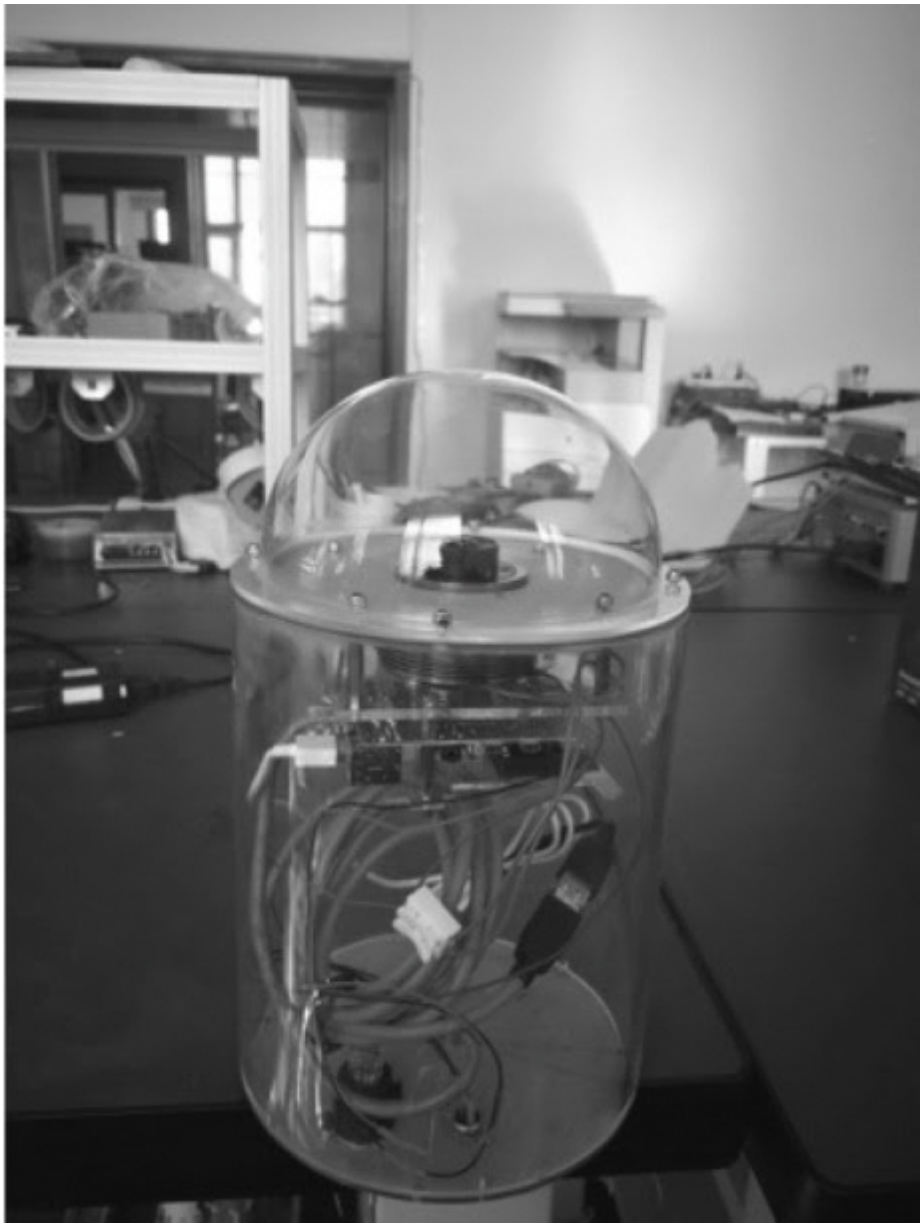

Figure 3: Figure 4

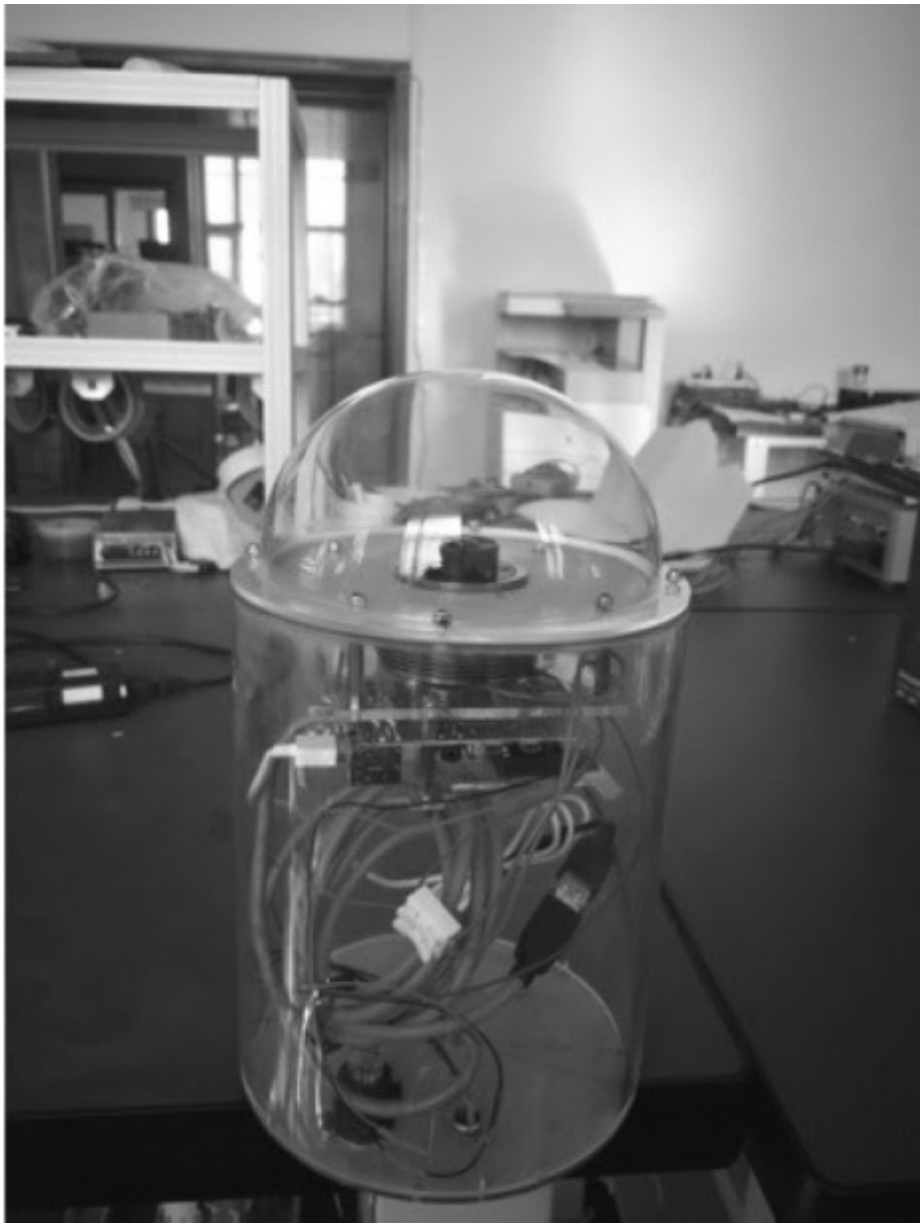

Figure 4: Figure 4

plane. This indicates that 13CO clumps containing C18O cores have a higher probability of appearing at b = 0°.

In FIGURE:7, the radial velocity center distribution of NM-type clumps is similar to that of M-type clumps. Based on the 0.25-0.75 quartile range of the statistical data, both are concentrated in the range (20, 45) km · s^{-1}. However, M-type clumps rarely appear at velocities less than -5 km · s^{-1} or greater than 75 km · s^{-1}. The small fraction of NM-type clumps appearing in the >75 km · s^{-1} range are located in more distant gas spiral arms where C18O detection cannot cover these regions.

3.2 Velocity Span

FIGURE:7 presents the probability density distributions of velocity spans for M-type and NM-type clumps, where velocity span is defined as the difference between the maximum and minimum velocities of a clump. For M-type clumps, the velocity span ranges from 2.66 to 10.13 km · s^{-1}, with most sources (0.25-0.75 quartile) falling in the range 4.82-6.14 km · s^{-1}. For NM-type clumps, the velocity span ranges from 1.36 to 18.58 km · s^{-1}, concentrated (0.25-0.75 quartile) in the range 3.65-4.82 km · s^{-1}. This indicates that M-type clumps have larger velocity spans.

3.3 Peak Intensity

FIGURE:8 shows the differences in peak intensity between M-type and NM-type clumps. For M-type clumps, the peak intensity distribution ranges from 3.53 to 30.71 K, while for NM-type clumps it ranges from 1.36 to 18.58 K. Compared to NM-type clumps, the peak intensity distribution of M-type clumps is shifted overall to higher values. The median peak intensity is 7.62 K for M-type and 3.40 K for NM-type, a difference of nearly 55%. Additionally, the mean peak intensity of M-type clumps is 4.61 K higher than that of NM-type clumps, indicating that M-type clumps have greater peak intensities.

3.4 Flux

The flux distribution is shown in FIGURE:8. The median flux value for M-type clumps is 1363.32 K · km · s^{-1}, which is 3.83 times that of NM-type clumps (355.95 K · km · s^{-1}). The mean flux for M-type clumps is 1755.00 K · km · s^{-1}, significantly greater than the 469.21 K · km · s^{-1} for NM-type clumps. We also calculated the total flux for all clumps. The total flux of all 7,097 13CO clumps is 1.01$×10^{7}$ K · km · s^{-1}, with the M-type clumps (accounting for only 5.97% of the total number) contributing 20% of the total flux (2.02$×10^{6}$ K · km · s^{-1}).

4 Morphological Parameter Analysis

4.1 13CO Clump Morphology

4.1.1 Eccentricity Real 13CO clumps have irregular shapes, while the ideal model for clumps is a three-dimensional Gaussian, which projects as an ellipse in two dimensions. Therefore, we performed ellipse fitting on the two-dimensional projections of 13CO clumps and used eccentricity as a reference indicator for shape. Eccentricity is an important parameter describing ellipse shape, reflecting its degree of flattening with values ranging from 0 to 1. The procedure consists of: (1) integrating each 13CO clump' s mask data along the velocity direction to obtain the two-dimensional boundary contour for ellipse fitting; (2) using the Ellipse function from the matplotlib.patches library to complete the contour fitting; (3) calculating eccentricity from the output major axis (a) and minor axis (b) according to the formula $E = \sqrt{(1 - b^2/a^2)}$.

FIGURE:9 shows an example of successful 13CO clump contour fitting. We examined all fitting results and found that 11 out of 7,097 13CO clumps (0.2%) failed to fit, with 9 of these from NM-type clumps. The fitting failures occurred because these clump contours were too irregular and deviated significantly from the elliptical model, as shown in FIGURE:9. Due to their small proportion, these 11 clumps were excluded from the statistical analysis without affecting the conclusions.

We compared the eccentricities of the two categories, with statistical distributions shown in FIGURE:10. Both have similar eccentricity ranges: 0.24-0.89 for M-type and 0.11-0.95 for NM-type, with M-type clumps showing more concentrated distributions. The median eccentricity is 0.64 for M-type and 0.67 for NM-type, with similar relationships for the mean values.

4.1.2 Angular Area Angular area (S) describes the size of clumps (actual sizes are strongly distance-dependent; here we discuss only the raw detection results). We define angular area as the pixel resolution (0.25 $arcmin^2$) multiplied by the number of pixels (Pixelnum) in the velocity-integrated projection of the masked clump on the two-dimensional plane: $S = 0.25 \times$ Pixelnum.

In FIGURE:10, M-type clumps have angular areas ranging from 30.75 to 227.5 $arcmin^2$, concentrated in the range 65.25-107.56 $arcmin^2$. NM-type clumps range from 14.0 to 255.25 $arcmin^2$, mainly in the range 45.75-77.0 $arcmin^2$. The former is about 30% larger in median value. Based on the distribution and median/mean values, M-type clumps have larger angular areas.

4.1.3 Form Factor Form Factor (FF) is a quantitative parameter describing object shape, where $FF = 1$ for a perfect circle and $FF < 1$ for deviations. The closer the value is to 1, the more circular the gas structure. The calculation is: $FF = 4\pi A/C^2$, where A is area and C is perimeter. We used the polygonarea and polygonlength functions from the shapely library to obtain area and perimeter for calculating 13CO clump form factors.

The form factor distribution is shown in FIGURE:10. Both categories have a median of 0.57. For the concentrated distribution interval, M-type clumps range from 0.51 to 0.63, while NM-type range from 0.50 to 0.60. The two categories are very similar, indicating that 13CO clump form factors do not differ significantly based on the presence of C18O cores.

4.2 Morphology of 13CO Clumps and C18O Cores

13CO is generally optically thin, making it suitable for tracing dense molecular clumps, while completely optically thin C18O can trace even smaller or denser regions. We also compared the morphologies of sources traced by different density probes by calculating form factors for M-type 13CO clumps and C18O cores. The distribution is shown in FIGURE:10, where Gaussian curves were fitted to the histograms with and σ representing the fitted mean and standard deviation. The form factors show clear differences between the two density probes.

The fitted parameters are = 0.56 for M-type 13CO clumps and = 0.82 for C18O cores, indicating that C18O cores are more circular in morphology within 13CO clumps. In summary, molecular cores are overall smaller and more circular than M-type clumps, representing more regular high-density substructures within 13CO clumps.

5 Conclusions

In the MWISP survey region of $10° \leq l \leq 20°$, we classified 13CO molecular clumps based on the presence or absence of C18O cores. The main conclusions are:

Among the 7,097 13CO molecular clumps, 424 contain C18O cores (M-type clumps), while the remaining 13CO clumps are NM-type. Specifically, 78% of 13CO clumps have one C18O core, 17% have two C18O cores, and the remaining 5% have more than two C18O cores. 13CO clumps containing C18O cores generally have larger velocity spans, peak intensities, and fluxes. In the entire 13CO clump sample, M-type clumps (accounting for only 5.97% of the total number) contribute 20% of the total flux. M-type and NM-type clumps show slight differences in morphological parameters. In terms of eccentricity, both categories have mean values greater than 0.5, confirming that elliptical models are reasonable for describing 13CO clumps in two dimensions. From angular area analysis, the former is about 30% larger in median value than the latter, indicating that larger 13CO clumps are more likely to form denser C18O cores within them. In terms of form factor, C18O cores within 13CO clumps have more regular morphologies—13CO clumps are more elliptical while C18O cores are more circular. This pattern suggests that higher-density molecular probes detect more regular structures, possibly indicating that gravity plays an increasingly important role in molecular core formation as density increases.

Acknowledgments

The data used in this research come from the Milky Way Imaging Scroll Painting survey. MWISP is a CO, 13CO, and C18O multi-line survey of the northern Galactic plane conducted with the Purple Mountain Observatory 13.7 m telescope. We are deeply grateful to all members of the MWISP survey team, especially the staff at the Qinghai Observatory, for their long-term efforts.

References

Blitz L, Stark A A. ApJ, 1986, 300: L89
Rosolowsky E W, Pineda J E, Foster J B, et al. ApJS, 2008, 175: 509
Ballesteros-Paredes J, André P, Hennebelle P, et al. SSRv, 2020, 216: 5
Gomez G C, Vazquez-Semadeni E. ApJ, 2014, 791: 124
Shu F H, Adams F C, Lizano S. ARA&A, 1987, 25: 23
Bontemps S, Motte F, Csengeri T, et al. A&A, 2010, 524: A18
Wilson R W, Jefferts K B, Penzias A A. ApJ, 1970, 161: L43
Bolatto A D, Wolfire M, Leroy A K. ARA&A, 2013, 51: 207
孙锦, 李守中. 分子天体物理学基础. 北京: 北京师范大学出版社, 2004: 12-15
Bo R, Jewitt D, Keil K. Protostars & Planets V//Francesco J D, Evans- N J, Caselli P, et al. An Observational Perspective of Low-Mass Dense Cores I: Internal Physical and Chemical Properties. Tucson: University of Arizona Press, 2006: 17
Lada C J, Muench A A, Rathborne J, et al. ApJ, 2008, 672: 410
Mark H H, Thomas M D. ARA&A, 2015, 53: 583
Dame T M, Hartmann D, Thaddeus P. ApJ, 2001, 547: 792
Jackson J M, Rathborne J M, Shah R Y, et al. ApJS, 2006, 163: 145
Rigby A J, Moore T J T, Plume R, et al. MNRAS, 2016, 456: 2885
Schuller F, Csengeri T, Urquhart J S, et al. A&A, 2017, 601: 25
Su Y, Yang J, Zhang S B, et al. ApJS, 2019, 240: 9
Yuan L X, Yang J, Du F J, et al. ApJS, 2021, 257: 51
Neralwar K R, Colombo D, Duarte-Cabral A, et al. A&A, 2022, 663: A56
Jaffa S E, Whitworth A P, Clarke S D, et al. MNRAS, 2018, 477: 1927
Clarke S D, Jaffa S E, Whitworth A P. MNRAS, 2022, 516: 2782
Stutzki J, Guesten R. ApJ, 1990, 356: 513
Williams J P, de Geus E J, Blitz L. ApJ, 1994, 428: 693
Berry D S. A&C, 2015, 10: 22
Rosolowsky E W, Pineda J E, Kauffmann J, et al. ApJ, 2008, 679: 1338
Maity A K, Dewangan L K, Sano H, et al. ApJ, 2022, 934: 2
Luo X Y, Zheng S, Huang Y, et al. RAA, 2022, 22: 125
Messineo M, Clark J S, Figer D F, et al. ApJ, 2015, 805: 110
Jiang Y, Zheng S, Jiang Z B, et al. A&C, 2022, 40: 100563
Oswalt T D, Gilmore G. Planets, Stars and Stellar Systems. Volume 5: Galactic Structure and Stellar Populations//Kroupa P, Weidner C, Pflamm-Altenburg J, et al. The Stellar and Sub-Stellar Initial Mass Function of Simple and Composite Populations. Heidelberg: Springer, 2013: 115

Jiang Y, Chen Z W, Zheng S, et al. ApJS, 2023, 267: 32
Luo X Y, Zheng S, Jiang Z B, et al. RAA, 2024, 24: 015021
Shan W L, Yang J, Shi S C, et al. ITTST, 2012, 2: 593
孙继先, 逯登荣, 杨戟, 等. 天文学报, 2018, 59: 3
李振强, 张旭国, 徐烨, 等. 天文学报, 2021, 62: 24
Hill T, Motte F, Didelon P, et al. A&A, 2012, 542: 791
Chen Z W, Sun W, Chini R, et al. ApJ, 2021, 922: 90
辛科霆, 安东升, 谢基伟, 等. 天文学报, 2023, 64: 46
Shin K T, An D S, Xie J W, et al. ChA&A, 2024, 48: 1
申洪, 朴英杰. 中国体视学与图像分析, 1999, 4: 10